Trace element partitioning between ilmenite, armalcolite and anhydrous silicate melt: Implications for the formation of lunar high-Ti mare basalts

van Kan, M.; Mason, P.R.D.; van Westrenen, W.

published in
Geochimica et Cosmochimica Acta
2011

DOI (link to publisher)
10.1016/j.gca.2011.04.031

document version
Publisher's PDF, also known as Version of record

Available online at www.sciencedirect.com
ScienceDirect
Geochimica et Cosmochimica Acta 75 (2011) 4179–4193
Geochimica et Cosmochimica Acta
www.elsevier.com/locate/gca

Trace element partitioning between ilmenite, armalcolite and anhydrous silicate melt: Implications for the formation of lunar high-Ti mare basalts

Mirjam van Kan Parker [a], Paul R.D. Mason [b], Wim van Westrenen [a,*]

[a] Faculty of Earth and Life Sciences, VU University Amsterdam, De Boelelaan 1085, 1081 HV Amsterdam, The Netherlands
[b] Faculty of Geosciences, Utrecht University, Budapestlaan 4, 3584 CD Utrecht, The Netherlands

Received 30 September 2010; accepted in revised form 27 April 2011; available online 6 May 2011

Abstract

We performed a series of experiments at high pressures and temperatures to determine the partitioning of a wide range of trace elements between ilmenite (Ilm), armalcolite (Arm) and anhydrous lunar silicate melt, to constrain geochemical models of the formation of titanium-rich melts in the Moon. Experiments were performed in graphite-lined platinum capsules at pressures and temperatures ranging from 1.1 to 2.3 GPa and 1300–1400 °C using a synthetic Ti-enriched Apollo 'black glass' composition in the CaO–FeO–MgO–Al_2O_3–TiO_2–SiO_2 system. Ilmenite–melt and armalcolite–melt partition coefficients (D) show highly incompatible values for the rare earth elements (REE) with the light REE more incompatible compared to the heavy REE ($D_{La}^{Ilm-melt}$ 0.0020 ± 0.0010 to $D_{Lu}^{Ilm-melt}$ 0.069 ± 0.010 for ilmenite; $D_{La}^{Arm-melt}$ 0.0048 ± 0.0023 to $D_{Lu}^{Arm-melt}$ 0.041 ± 0.008 for armalcolite). D values for the high field strength elements vary from highly incompatible for Th, U and to a lesser extent W (for ilmenite: $D_{Th}^{Ilm-melt}$ 0.0013 ± 0.0008, $D_{U}^{Ilm-melt}$ 0.0035 ± 0.0015 and $D_{W}^{Ilm-melt}$ 0.039 ± 0.005, and for armalcolite $D_{Th}^{Arm-melt}$ 0.008 ± 0.003, $D_{U}^{Arm-melt}$ 0.0048 ± 0.0022 and $D_{W}^{Arm-melt}$ 0.062 ± 0.03), to mildly incompatible for Nb, Ta, Zr, and Hf (e.g. $D_{Hf}^{Ilm-melt}$ 0.28 ± 0.05 and : $D_{Hf}^{Arm-melt}$ 0.76 ± 0.07). Both minerals fractionate the high field strength elements with D_{Ta}/D_{Nb} and D_{Hf}/D_{Zr} between 1.3 and 1.6 for ilmenite and 1.3 and 1.4 for armalcolite. Armalcolite is slightly more efficient at fractionating Hf from W during lunar magma ocean crystallisation, with $D_{Hf}/D_{W} = 12–13$ compared to 6.7–7.5 for ilmenite. The transition metals vary from mildly incompatible to compatible, with the highest compatibilities for Cr in ilmenite ($D \sim 7.5$) and V in armalcolite ($D \sim 8.1$). D values show no clear variation with pressure in the small range covered.

Crystal lattice strain modelling of D values for di-, tri- and tetravalent trace elements shows that in ilmenite, divalent elements prefer to substitute for Fe while armalcolite data suggest REE replacing Mg. Tetravalent cations appear to preferentially substitute for Ti in both minerals, with the exception of Th and U that likely substitute for the larger Fe or Mg cations. Crystal lattice strain modelling is also used to identify and correct for very small (~0.3 wt.%) melt contamination of trace element concentration determinations in crystals.

Our results are used to model the Lu–Hf–Ti concentrations of lunar high-Ti mare basalts. The combination of their subchondritic Lu/Hf ratios and high TiO_2 contents requires preferential dissolution of ilmenite or armalcolite from late-stage, lunar magma ocean cumulates into low-Ti partial melts of deeper pyroxene-rich cumulates.

1. INTRODUCTION

The elemental and isotopic compositions of the main rock suites on the lunar surface are commonly interpreted in the general framework of the lunar magma ocean (LMO) model (Smith et al., 1970; Wood et al., 1970). This

* Corresponding author. Tel.: +31 20 5987279; fax: +31 20 5989942.
E-mail address: wim.van.westrenen@falw.vu.nl (W. van Westrenen).

0016-7037/$ - see front matter © 2011 Elsevier Ltd. All rights reserved.
doi:10.1016/j.gca.2011.04.031

model invokes the presence of a compositionally and mineralogically layered interior early in the evolution of the Moon, formed by cooling and crystallisation of a global magma ocean (e.g. Snyder et al. 1992; Shearer et al., 2006; Elardo et al., 2011).

In the context of the LMO model, lunar mare basalts are thought to be partial melts of layered lunar mantle cumulates. For example, trace element depleted basalts are interpreted to originate from deep, early-formed olivine- and pyroxene-bearing cumulates that sank to the bottom of the LMO (e.g. Münker, 2010; van Kan Parker et al., 2011 and references therein). Uniquely Ti-rich basalts, with TiO_2 contents up to ~14 wt.% (e.g., Neal and Taylor, 1992; Shearer et al., 2006), have also been interpreted in the framework of the LMO model, by invoking a role for late-stage LMO cumulates rich in the Ti-rich mineral ilmenite (nominally (Fe,Mg)TiO_3) and/or armalcolite (Fe,Mg)-Ti_2O_5) in their genesis (e.g. Longhi, 1992; Snyder et al., 1992; Shearer et al., 1996, and references therein). Ilmenite is also a possible candidate for causing the observed fractionation of W from Hf during lunar magma ocean crystallisation (e.g. Shearer and Papike, 1999; Lee et al., 2002; Klemme et al., 2006).

Petrological modelling and high-pressure experiments show that ilmenite and armalcolite are indeed expected to become stable phases during the latest stages of LMO crystallisation (Snyder et al., 1992; Thacker et al., 2009). Their presence at relatively shallow levels combined with their relatively high density (e.g. Tronche et al., 2010) is thought to have resulted in a gravitationally unstable mineral stratification in the lunar mantle, inducing a mantle overturn that triggered significant mare basalt formation (e.g. Elkins-Tanton et al., 2002; Hess and Parmentier, 1995; de Vries et al., 2010).

Although the involvement in ilmenite and/or armalcolite in high-Ti basalt generation is fully accepted, the processes leading to the Ti enrichment are subject to debate (e.g. Shearer and Papike, 1999; Elkins-Tanton et al., 2002; Münker, 2010). Some models propose direct melting of ilmenite-rich cumulates after convective mantle overturn (e.g. Ringwood and Kesson, 1976; Hess and Parmentier, 1995; Beard et al., 1998). Other scenarios involve hybridization of low-Ti melts by assimilation of ilmenite/armalcolite and clinopyroxene-rich cumulates (e.g., Hubbard and Minear, 1975; Wagner and Grove, 1997; Liang et al., 2007; Liang and Hess, 2008).

Geochemical models attempting to identify the roles of these different processes in high-Ti basalt formation (e.g. Münker, 2010) require accurate knowledge of major and trace element partitioning between ilmenite, armalcolite, and lunar melts during partial melting and crystallisation processes at high pressure (P) and temperature (T) conditions. Previously published studies reporting ilmenite–melt and/or armalcolite-melt partition coefficients (D, defined as the ratio by weight between elemental concentrations in mineral and co-existing melt) show large variations in measured D values, varying up to three orders of magnitude for ilmenite and one order of magnitude for armalcolite (Green et al., 1971; McKay and Weill, 1976; Palme and Wlotzka, 1977; Irving et al., 1978; Fujimaki and Tatsumoto, 1984; McKay et al., 1986; Nakamura et al., 1986; Candela and Bouton, 1990; LaTourrette et al., 1991; Stimac and Hickmott, 1994; Zack and Brumm, 1998; Righter and Shearer, 2003; Klemme et al., 2006).

These variations, that must be related to a combination of the range of natural and synthetic compositions (x) used, and differences in the P, T and oxygen fugacity (fO_2) conditions applied, make it very difficult to identify appropriate D values for petrogenetic modelling of lunar melting and crystallisation processes involving these minerals. The lack of systematic data specifically tailored to lunar P–T–x conditions also precludes development of predictive partitioning models for use in studies of lunar petrogenesis. Here we present a series of ilmenite–melt and armalcolite–melt partition coefficients for large ion lithophile elements (LILE) Li and Ba; rare earth elements (REE), La, Ce, Nd, Sm, Eu, Er, Tm, Y, Yb, and Lu; high field strength elements (HFSE) Zr, Nb, Hf, Ta, Th and U; and transition metals Sc, V, Mn, Co, Cu, and Mo, derived from experiments performed in a synthetic lunar basaltic composition at temperatures between 1300 and 1400 °C, P between 1.1 and 2.3 GPa and relatively reducing conditions. The wide range of trace elements that were added allows us to assess the applicability of the crystal lattice strain model (Blundy and Wood, 1994) to ilmenite–melt and armalcolite–melt partitioning data, providing a step towards the development of fully predictive partitioning models. We illustrate the relevance of our new data by assessing the roles of ilmenite and armalcolite in determining the Lu–Hf–Ti concentrations of high-Ti lunar mare basalts.

2. METHODS

2.1. Experimental and analytical techniques

Experiments were performed in the CaO–FeO–MgO–Al_2O_3–TiO_2–SiO_2 system (CFMATS). The starting mixture and experimental P–T conditions were guided by the study of Beck and Hess (2004), who mapped the solubility of ilmenite in a synthetic high-Ti Apollo red glass. Our starting mixture (Table 1) was chosen to be a synthetic Ti-enriched high-Ti Apollo black glass equivalent (Delano, 1986).

The starting material was prepared by mixing appropriate amounts of high purity (99.5–99.99%, Alfa Aesar) powdered oxides (MgO, Fe_2O_3, Al_2O_3, TiO_2, SiO_2) and $CaCO_3$ (99.95–100.05%, Alfa Aesar). The oxides MgO, Al_2O_3, TiO_2 and SiO_2 were fired overnight at 1000 °C prior to use to drive off residual moisture, and subsequently stored at 110 °C, as were Fe_2O_3 and $CaCO_3$. After mixing the starting material under ethanol in an agate mortar for 1 h, it was dried in air and decarbonated in a Pt crucible in a box furnace by gradually raising T from 650 to 1200 °C over 7.5 h. The Pt crucible had previously been iron-saturated to minimize Fe loss during starting composition preparation. The mixture was subsequently melted at 1550 °C for 10 min and quenched by immersing the bottom of the Pt crucible in water. A small chip of the resulting glass was embedded in epoxy, polished, carbon coated and analysed for homogeneity by electron microprobe.

Table 1
Major element composition (in wt.%) of average Apollo 14 black (A14) glass (Delano, 1986) and of the synthetic six-component starting material (SM) used in this study. *n.* denotes the number of microprobe analysis used to determine the SM composition.

	n.	SiO_2	TiO_2	Al_2O_3	Cr_2O_3	FeO	MgO	MnO	CaO	Na_2O	K_2O	Total
A14		34.0	16.4	4.6	0.92	24.5	13.3	0.31	6.9	0.23	0.16	101.32
SM	6	30.4(4)	25.3(3)	4.18(6)	-	21.7(2)	11.7(1)	-	6.33(8)	-	-	99.6(2)

Numbers in parentheses indicate one standard deviation (1σ) of replicate analyses in terms of last significant numbers: 30.4(4) should be read as 30.4 ± 0.4.

Table 2
Summary of experimental conditions and run products. Run products from experiments in bold were selected for trace element concentration analysis. Abbreviations: ilm: ilmenite; gk: geikielite; arm: armalcolite; opx: orthopyroxene; rut: rutile; cpx: clinopyroxene, tr: trace. Typical error in calculated abundances is 2%.

Run	Temperature (°C)	Pressure (GPa)	Time (h)	Modal abundances[b]
1	**1300**	**1.1**	**26**	**16% Ilm/Gk, 5% Arm, 18% Opx, 61%melt**
2[a]	1300	1.1	26	100% melt
3	**1305**	**1.4**	**24**	**17% Ilm/Gk, 1% Arm, 18% Opx, 64% melt**
4	**1315**	**1.7**	**23**	**20% Ilm/Gk, 23% Opx, tr Rut, 57% melt**
5	1300	2.25	22.75	32% Ilm/Gk, 5% Rut, 55% Cpx + Opx, 8% melt
6	1325	2.25	26	32% Ilm/Gk, 4% Rut, 50% Cpx + Opx, 14% melt
7	1350	2.25	26	9% Rut, 18% Opx, 73% melt
8	1400	2.25	23	13% Opx, tr Rut, 86% melt

[a] Only Pt capsule was used, no inner graphite capsule.
[b] Modal abundances calculated using mass balance of starting material (Table 1) and phase compositions (Table 3).

The glass was ground under ethanol in an agate mortar for 1 h and doped with varying amounts of the LILE Li and Ba; the REE La, Ce, Nd, Sm, Eu, Er, Tm, Y, Yb, and Lu; the HFSE Zr, Nb, Hf, Ta, Th and U; and transition metals Sc, V, Mn, Co, Cu, and Mo, using 1000 ppm atomic absorption spectroscopy (AAS) standard solutions. The total amount of added trace elements was <0.25 wt.% for experiment 1 and <0.70 wt.% for all other experiments. The resulting mixture was remelted for 10 min at 1550 °C to promote starting material homogeneity for major and trace elements. The starting material was ground under ethanol one final time for 1 h in an agate mortar, dried in air and stored at 110 °C.

Table 2 gives an overview of experimental conditions used in this study. High *P*–*T* experiments were conducted in an end-loaded piston-cylinder (PC) at the Faculty of Earth and Life Sciences, VU University Amsterdam, using a ½ in. diameter talc-Pyrex cell assembly. The assembly was calibrated via the albite to jadeite plus quartz and fayalite to ferrosilite plus quartz transitions at 1000 °C, resulting in a pressure correction due to friction of 3% and pressure uncertainty of 0.1 GPa. A hand-machined graphite bucket, with an ID of 0.7 mm, OD of ~1.7 mm and length of 3–4 mm, was filled, closed with a graphite lid and inserted in a Pt capsule, with an ID of 1.7 mm, OD 2.0 mm, and length of 5–7 mm. The bottom of the Pt capsule was triple crimped, flattened and welded shut at one end, after the graphite capsule was inserted the other end was crimped and welded shut using a Lampert PUK 3 welder. Before closing and welding shut, the capsules were held at 575 °C for ~10 min to drive off residual moisture.

A Pt-graphite double capsule was chosen to impose a relatively low oxygen fugacity (fO_2) of approximately 1.5 log units above the iron–wüstite buffer (IW + 1.5, Médard et al., 2008), reasonably close to fO_2 estimates for the lunar mantle (~ IW-0.6, Nicholis and Rutherford, 2009). Oxygen fugacity has been shown to affect phase relations in lunar mantle compositions (e.g. Krawczynski and Grove, 2008), and can influence mineral–melt partitioning behaviour by affecting the dominant valence state of multivalent elements such as Eu, Fe, Cr, Ti, and V (e.g. Papike et al., 2005), by enabling or disabling coupled substitutions that accompany heterovalent substitutions in mineral structures (for example those involving Fe^{3+}).

T was monitored and controlled during experiments using a $W_{97}Re_3$-$W_{75}Re_{25}$ (type D) thermocouple and Eurotherm 2404 controller, with a resulting *T* uncertainty of ±3°. The centre of the sample was located in the hotspot of the assembly, ~2 mm away from the thermocouple tip end. This ensured *T* in all parts of the samples to remain within 10 °C of the thermocouple readings (Watson et al., 2002). The 'hot piston in' technique was used to bring the sample to the desired *P*–*T* conditions. Experiments were terminated by shutting off the power to the furnace.

Experimental run products were mounted in epoxy resin, polished and carbon coated for electron microprobe analysis. Glasses and crystals were analysed for major elements with a JEOL JXA 8800M electron microprobe at VU University Amsterdam. The accelerating voltage was 15 kV at a beam current of 25 nA. For the glass analysis we used a defocused beam of 10 μm diameter. A focused beam of 0.5 μm diameter was used for the mineral phases. Analyses were calibrated against primary standards diopside (Mg, Si, Ca), ilmenite (Ti, Fe), and corundum (Al). A natural MORB glass (for Mg, Al, Si, Ca and Fe), diopside (for Mg, Ca, and Al) and ilmenite (for Ti) were used

as secondary standards. Peak and background count times were 25 and 25 s (2 × 12.5 s), respectively, while iron was measured using 36 and 36 s (2 × 18 s). Data were corrected according to the ZAF algorithm (Reed, 2005).

Trace element concentrations in crystals and glasses in experiments that contained >50% by mass of silicate melt were determined by laser ablation inductively coupled mass spectrometry (LA-ICP-MS) at Utrecht University. The LA-ICP-MS system consists of a 193-nm GeoLas 200Q Excimer laser ablation system (Günther et al., 1997) coupled to a Thermo Finnigan Element 2 sector field ICP-MS instrument, operated in low-resolution mode. Samples were ablated to produce 20 or 30 μm diameter craters, dependent on crystal size. Trace element concentrations of the glasses were measured in 5–8 different spots. Five or six laser ablation spots were located on Ilm–Gk crystals and four or five on Arm crystals. Mixing between mineral and melt phases during laser ablation analysis was monitored using LREE concentrations and results that were clearly affected by mixing (due to poor targeting of the laser beam) were discarded. Measurements were also discarded when crystals could only be analysed for less than 10 s, i.e. when crystals proved to be too thin and too few laser scans could be used for averaging the values, resulting in large standard deviations for individual measurements).

A constant fluence of 5 J cm^{-2} was used with a pulse repetition rate of 5 Hz for both glass and co-existing minerals. Calibration was performed against NIST SRM 610 glass using the published values of Pearce et al. (1997). Ti concentrations as obtained by electron microprobe were used as internal standard. The following isotopes were measured ^{45}Sc, ^{47}Ti, ^{51}V, ^{53}Cr, ^{55}Mn, ^{59}Co, ^{63}Cu ^{89}Y, ^{90}Zr, ^{93}Nb, ^{95}Mo, ^{137}Ba, ^{139}La, ^{140}Ce, ^{146}Nd, ^{147}Sm, ^{153}Eu, ^{166}Er, ^{169}Tm, ^{172}Yb, ^{175}Lu, ^{178}Hf, ^{181}Ta, ^{182}W, ^{232}Th and ^{238}U, with typical ablation times of 60 s. Background intervals of 60 s were measured before and after ablation of the sample. Trace element concentrations determined for the USGS glass external standard Columbia River Basalt BCR2-G during our analytical sessions were typically within 20% of recommended values, as suggested in the GeoReM database (e.g. Jochum and Brueckner, 2008). Measured Er and Yb concentrations were generally >20% (up to 44%) higher than the GeoReM recommended values, but within 20% of the concentrations reported by Dorrit (2006) (3.19 and 3.25 ppm, respectively). As our focus is on determining accurate partition coefficients rather than accurate absolute concentrations in co-existing minerals and melts, these deviations are considered acceptable.

2.2. Lattice strain modelling

We used the crystal lattice strain model of Blundy and Wood (1994) to rationalise the measured mineral–melt partition coefficients. The model is based on the near-parabolic dependence of log(D) values for series of isovalent cations on cation radius, as first observed by Onuma et al. (1968). The model of Blundy and Wood (1994) describes mineral–melt trace element partition coefficients for a series of isovalent elements i ($D_i^{\text{mineral–melt}}$) with radii r_i entering a given crystal-structural site using three parameters: D_0, the maximum partition coefficient for a (fictive) element with ideal radius r_0 that imposes minimal strain on the crystal lattice when incorporated, and the site's apparent Young's modulus (E):

$$D_i^{\text{mineral–melt}} = D_0 \exp\left(\frac{-4\pi E N_A\left[\frac{1}{2}r_0(r_i - r_0)^2 + \frac{1}{3}(r_i - r_0)^3\right]}{RT}\right) \quad (1)$$

with N_A Avogadro's number and R the gas constant.

Ilmenite–geikielite (space group: $R\bar{3}$ is characterised by a hexagonal close-packed structure of oxygen atoms similar to the corundum structure, and consists of alternating layers of Ti- and Fe/Mg-containing octahedra (e.g. Raymond and Wenk, 1971). Both Fe/Mg and Ti lattice sites are sixfold coordinated. Armalcolite (space group: *Bbmm*) is a solid solution between ferropseudobrookite ($FeTi_2O_5$) and karrooite ($MgTi_2O_5$). Armalcolite has the pseudobrookite structure, made up of bands of distorted edge-sharing octahedra (e.g. Smyth, 1974) and is also characterised by two lattice sites referred to as the M1 site (occupied by Mg/Fe) and the M2 site (occupied by Ti), which are both sixfold coordinated. Sixfold coordinated radii of all elements were taken from Shannon (1976). Experimental results for nominally M^{2+}, M^{3+} and M^{4+}cations were fitted to Eq. (1), using a non-linear least square Levenberg–Marquardt fitting routine (Press et al., 1992). Data were weighted using the standard deviation on D as weighting factor and minimising $\chi^2 = \sum\left[(D_i^{\text{observed}} - D_i^{\text{calculated}})/D_i^{\text{observed}}\right]^2$.

3. RESULTS

3.1. Run products and evidence for equilibrium

Run products are listed in Table 2, and major element compositions of the co-existing mineral and melt phases are given in Table 3. An overview of the resulting phase assemblages at run conditions is shown in Fig. 1, with back-scattered electron images of run products shown in Fig. 2. Armalcolite co-exists with ilmenite and orthopyroxene at 1.1 GPa – 1300 °C and 1.4 GPa – 1305 °C (Fig. 1). Consistent with previous studies (Friel et al., 1977; Thacker et al., 2009) we find that at $P > 1.4$ GPa armalcolite is no longer stable. In five of the eight experiments (at pressures of 1.1 and 2.3 GPa) either no Ilm or Arm crystals were present (with rutile becoming the stable high-Ti phase towards higher P and T), or temperatures were so close to the solidus for this composition that the resulting low melt fraction (<15 wt.%) was mostly present in small melt pockets, precluding reliable D determinations.

With increasing P rutile co-exists with Ilm, orthopyroxene (Opx) and/or clinopyroxene. In the experiments at 2.3 GPa at $T > 1325$ °C clinopyroxene and Ilm are no longer stable. At $T > 1350$ °C the modal abundance of rutile decreases significantly and at 1400 °C Ti is distributed between the silicate melt and co-existing Opx.

Titanium-rich crystals are euhedral to subhedral and varied considerably in size within and between experiments with diameters between 10 and 100 μm. Orthopyroxene

Table 3
Summary of microprobe analyses (wt.%) of selected experiments, *n.* is number of microprobe analysis. Other abbreviations are as in Table 2. Rutile was not analysed.

Exp.	Mineral	*n.*	SiO_2	TiO_2	Al_2O_3	FeO	MgO	CaO	Total
1	Ilm	8	0.03(2)	57.9(2)	0.66(2)	32.3(1)	10.2(1)	0.11(3)	101.2(2)
	Arm	11	0.14(1)	73.3(5)	2.30(11)	15.8(1)	8.89(8)	0.17(7)	100.6(4)
	Opx	9	55.0(4)	1.69(17)	1.69(25)	13.2(3)	28.1(4)	1.52(17)	101.2(1)
	Melt	21	35.9(6)	20.0(7)	6.21(29)	20.4(3)	8.97(21)	9.63(27)	101.1(2)
3	Ilm	9	0.04(1)	57.0(2)	0.78(2)	32.3(2)	10.4()	0.08(1)	100.5(4)
	Arm	13	0.16(2)	71.9(4)	2.65(3)	16.0(3)	8.96(11)	0.13(9)	99.8(6)
	Opx	11	54.3(7)	1.53(12)	1.97(23)	13.7(1)	27.7(3)	1.72(15)	100.9(5)
	Melt	8	32.4(1)	22.6(2)	5.67(4)	20.9(2)	8.58(7)	8.71(11)	98.9(3)
4	Ilm	12	0.05(2)	57.3(3)	0.93(1)	33.1(2)	9.48(15)	0.12(3)	101.0(3)
	Opx	10	53.4(6)	1.63(23)	2.36(44)	14.3(2)	26.6(3)	2.22(9)	100.5(7)
	Rut	-							
	Melt	6	32.2(6)	23.7(5)	6.25(15)	21.1(6)	7.17(88)	9.68(20)	100.1(6)

Numbers in parentheses indicate one standard deviation (1σ) of replicate analyses in terms of last significant numbers: 0.03(2) should be read as 0.03 ± 0.02.

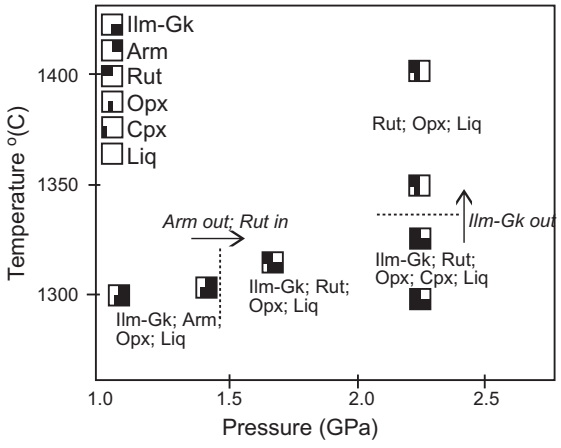

Fig. 1. Overview of the run conditions used in this study and resulting experimental products.

crystals generally also enveloped minute Ilm crystals, and showed poorly defined crystal faces.

Electron microprobe analyses of core–rim transects across grains revealed no major or minor element zonation. Small standard deviations of measurements in both minerals and melts (Table 3) show insignificant crystal-to-crystal compositional variations. The ilmenite crystals formed in the experiments were solid solutions between compositional end-members ilmenite ($FeTiO_3$) and geikielite (Gk; $MgTiO_3$) and are hereafter referred to as Ilm–Gk. Most lunar ilmenites are also Ilm–Gk solid solutions (e.g. Lucey et al., 2006). Mineral major element compositions do not vary significantly across the relatively limited *P–T* range covered in this study. At $P = 1.1$ GPa, $T = 1300$ °C, Ilm–Gk with composition $Ilm_{64.0}Gk_{36.0}$ coexists with Opx, $En_{76.8}Fs_{20.2}Wo_{3.0}$. At $P = 1.4$ GPa, $T = 1305$ °C, $Ilm_{63.6}Gk_{0.36.4}$ coexists with $En_{75.6}Fs_{21.0}Wo_{3.4}$ and finally at $P = 1.7$ GPa, $T = 1315$ °C, $Ilm_{66.2}Gk_{33.8}$ coexists with $En_{73.5}Fs_{22.1}Wo_{4.4}$.

Glasses were transparent and free of inclusions and bubbles. Locally the melt showed a slightly quenched texture (darker areas/spots in Fig. 2). Multiple laser ablation analyses both within larger individual Ilm–Gk and Arm grains, and in different crystals in a single run product resulted in comparable trace element concentrations, with no significant core to rim variations or within-sample heterogeneity, suggesting a close approach to equilibrium.

Additional evidence for major and trace element equilibration in our experiments comes from the results of a preliminary experiment identical in run conditions and run duration to experiment 3, that used a starting composition identical in major and minor element abundances to the composition used in experiments 1–8, but doped with lower concentrations of trace elements. Laser ablation analysis of the phases in this preliminary experiment revealed that concentrations of most trace elements in the resulting Ilm–Gk and Arm crystals were below detection limit, causing us to repeat the experiment at the higher doping levels reported here. However, doping levels in the preliminary experiment were sufficient to obtain precise Arm–melt *D* values for V, Cr, Zr, Nb and Ta. Resulting major, minor and trace element partition coefficients in this experiment are identical within 1–2σ to the results of experiment 3, providing strong evidence for equilibration.

This result is consistent with the results of previous time series studies of silicate mineral–silicate melt partitioning performed in several laboratories. Mysen et al. (2004) and Mysen and Shang (2005) showed that 24 h is sufficient to reach equilibrium for both major and trace elements at 1350–1400 °C in olivine–melt systems at 1 atm. Pertermann et al. (2004) reported no significant difference in garnet–melt trace element partitioning data in experiments at 1350 °C lasting 4, 15 or 24 h in a similar synthetic system at a pressure of 3 GPa.

3.2. Partition coefficients and lattice strain models

Major element partition coefficients show a minor decrease with increasing pressure in D_{Ti} for both Ilm–Gk, from 2.9 ± 0.1 (Exp. 1, 1.1 GPa) to 2.5 ± 0.1 (Exp. 3, 1.4 GPa) to 2.4 ± 0.1 (Exp 4, 1.7 GPa) and Arm, from 3.7 ± 0.1 (Exp. 1, 1.1 GPa) to 3.2 ± 0.1 (Exp. 3, 1.4 GPa).

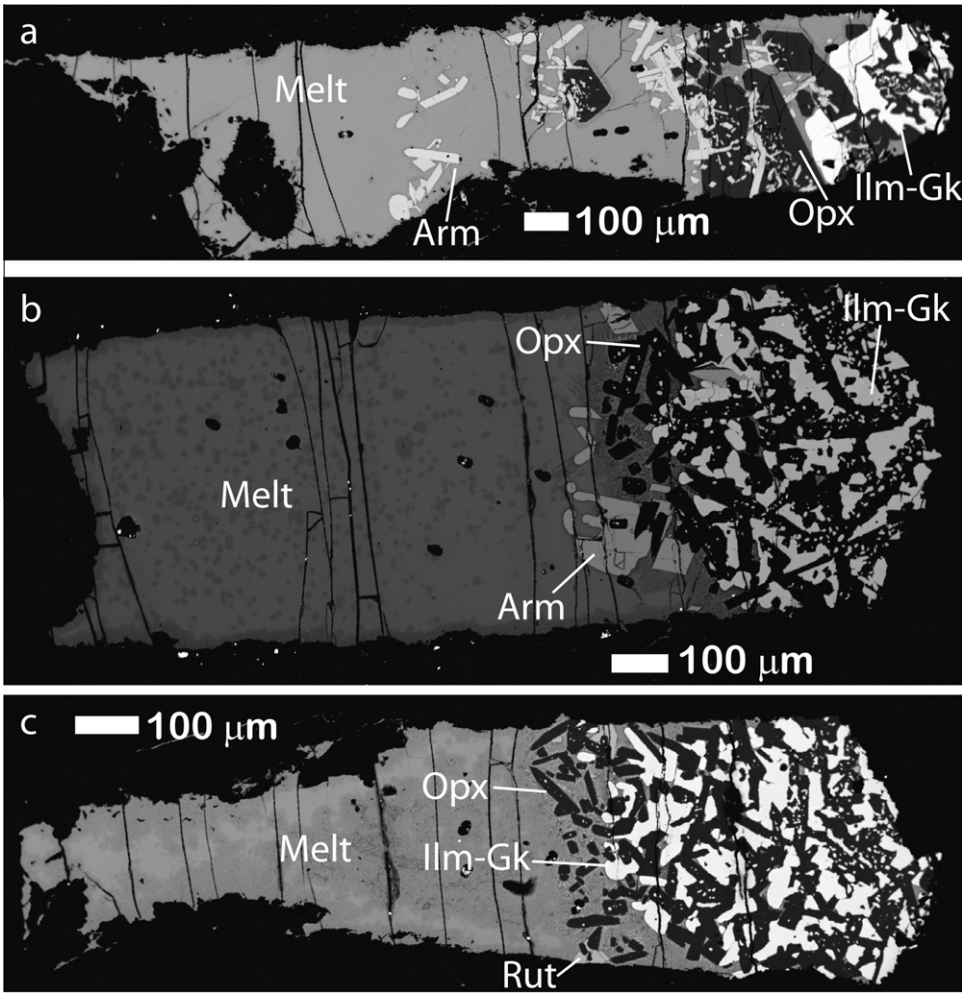

Fig. 2. Back-scattered electron (BSE) microprobe images of experiments in which ilmenite formed (a) experiment 1 at $P = 1.1$ GPa, T = 1300 °C; (b) Experiment 3 at $P = 1.4$ GPa, $T = 1305$ °C, (c) Experiment 4 at $P = 1.7$ GPa, $T = 1315$ °C. Thermocouple junction (top of capsule) is towards the left of the picture in all cases. Vertical cracks are due to decompression after completion of the experiments. All experiments contain varying amounts of Ilmenite–Geikelite (Ilm/Gk) crystals and orthopyroxene (Opx), additionally experiments 1 and 3 contain armalcolite (Arm). Experiment 4 contains trace amounts of rutile (Rut). Darker patches are areas where the melt showed a slightly quenched structure.

Mg is compatible in both Ilm–Gk ($D = 1.1$–1.3 ± 0.1) and Arm ($D = 1.0 \pm 0.1$), whereas Fe is compatible in Ilm–Gk ($D = 1.5$–1.6 ± 0.1) and slightly incompatible in Arm ($D = 0.76$–0.78 ± 0.01).

All trace element concentrations in minerals and co-existing melts are summarised in Table 4. We were unable to use any of the analysis performed on Ilm–Gk minerals of experiment 4 at 1.7 GPa and 1315 °C since the mineral analyses were clearly affected by mixing, but for completeness the average glass composition for this experiment is given in Table 4.

Trace element concentrations show very small variations within the different run product phases with standard deviations typically ~10% of the average value (Table 4). Higher concentrations (e.g. >10 ppm) on average correlate with smaller standard deviations (<10%), while low concentrations (e.g. <1 ppm) show standard deviations of ~30%. Uncertainties for the HREE and Th can be higher, with standard deviations of up to 65% for Th in Ilm–Gk (Experiment 1).

Resulting mineral–melt partition coefficients for Ilm–Gk and Arm are listed in Table 5. In Fig. 3 our results are compared to literature data for both Ilm–Gk and Arm. Our Ilm–Gk D values are generally towards the lower end of the wide range in reported literature values, in particular for the HFSE. Armalcolite values are also generally at the lower end of the reported literature data range, however, there is less agreement and the literature D range is smaller, due to the limited number of studies dealing with the partitioning behaviour of Arm. Our results are consistent with the recent study of Ilm–Gk/melt partitioning by Dygert et al. (2011), who show a decrease in HFSE (Zr, Hf, Nb, Ta) D values with increasing melt TiO_2 content. Dygert et al. (2011) attribute this decrease in terms of HFSE substitutions for tetravalent Ti (charge-balanced by trivalent cations in case of Nb and Ta) in high-Ti melts. In this case,

Table 4
Measured trace element concentrations (in ppm) by laser ablation from melt and crystals, *n.* stands for number of analyses. Ti was used as internal standard.

Exp.	1			3			4
Phase	Melt	Ilm/Gk	Arm	Melt	Ilm/Gk	Arm	Melt
n.	5	5	3	6	3	3	8
Sc	27(2)	25(2)	44(2)	313(12)	228(6)	471(14)	321(29)
V	31(6)	133(9)	290(26)	64(5)	267(21)	440(32)	66(7)
Cr	60(8)	428(28)	384(37)	58(7)	451(60)	388(54)	62(12)
Mn	80(12)	94(7)	27(1)	123(13)	132(33)	41(13)	142(24)
Co	19(4)	48(2)	24(1)	61(9)	143(49)	64(12)	64(11)
Cu	2.3(4)	6.9(1)	9.2(6)	1.7(5)	4.0(4)	3.8(8)	-
Y	36(4)	0.88(23)	0.70(36)	227(28)	2.8(2)	1.9(4)	296(34)
Zr	44(4)	10(1)	26(3)	116(14)	19(2)	63(7)	161(16)
Nb	33(4)	17(2)	23(1)	94(11)	38(1)	63(10)	123(12)
Mo	39(4)	36(8)	34(5)	170(24)	101(10)	117(23)	194(19)
Ba	320(45)	1.1	3.3(10)[a]	545(64)	0.75	1.7(1)	740(68)
La	162(22)	0.48(18)[b]	1.2(7)[a]	432(44)	0.44(15)[a]	1.1(2)	575(48)
Ce	124(18)	0.24(16)	1.2(5)[a]	344(39)	0.21(14)	1.0(2)	448(40)
Nd	79(8)	BD < 0.19	0.67(16)[a]	338(36)	0.26(13)	1.1(4)	451(49)
Sm	42(8)	0.37	BD < 0.30	236(27)	0.61(21)[a]	BD < 0.8	316(31)
Eu	46(9)	0.21(8)	0.58(14)[a]	247(33)	0.38(16)	0.69(20)	323(33)
Er	36(7)	1.1(4)	0.54(6)[a]	186(23)	3.5(5)	2.3(5)	244(31)
Tm	104(22)	4.6(10)	1.9(2)[a]	181(17)	5.2(3)	2.9(1)	245(31)
Yb	81(17)	4.8(10)	2.3(4)	199(17)	8.9(11)	4.6(6)[a]	270(28)
Lu	72(12)	5.7(11)	3.5(12)	182(17)	11(1)	5.8(2)	252(28)
Hf	35(5)	11(0)	29(2)	111(9)	25(5)	77(8)	154(16)
Ta	29(2)	24(2)	29(1)	93(8)	58(7)	81(5)	103(10)
W	126(19)	5.5(10)	8.2(13)[a]	458(53)	16(1)	27(4)	604(49)
Th	396(69)	0.82(54)	2.8(13)[a]	963(103)	0.42(22)[a]	2.5(6)	1369(95)
U	237(38)	1.2(5)	2.5(7)[a]	334(35)	0.63(15)	1.5(3)	445(23)

Numbers in parentheses indicate one standard deviation (1σ) of replicate analyses in terms of last significant numbers: 27(2) should be read as 27 ± 2. When a value lacks 1σ then only 1 measurement was above the detection limit. BD = below detection limit.
[a] Indicates that 1 measurement was discarded, e.g. when $n = 5$ and a number is marked by 'a' only 4 measurements could be used.
[b] Two measurements were discarded.

HFSE melt activities increase with increasing TiO_2 content, lowering partition coefficients, as also observed in rutile–melt systems (e.g. Horng et al., 2000). Fig. 3 illustrates the necessity to use appropriate compositions and conditions in order to obtain reliable *D* values for lunar petrogenetic modelling.

The small set of *D* values presented by Dygert et al. (2011) was obtained at conditions and bulk compositions similar to ours, using starting material pre-conditioned at a more reducing fO_2 of IW-1. The close similarity between our Ilm–Gk/melt partition coefficients and the Dygert et al. (2011) data suggests that there is no significant difference in *D* values between our experiments at $fO_2 = IW + 1.5$ and experiments at fO_2 close to that of the lunar mantle (~IW-0.6, Nicholis and Rutherford, 2009).

Ilm–Gk/melt and Arm/melt partition coefficients, shown together in Fig. 4, are comparable but not identical. The LREE, Th and U are all preferentially incorporated into Arm, and display lowest partition coefficients. The HREE and W show intermediate partition coefficients and are generally preferentially incorporated into Ilm–Gk, apart from W in experiment 1 at 1.1 GPa and Tm in experiment 3 at 1.4 GPa, which have somewhat higher *D* values for Arm. The HFSE and Mo have partition coefficients near 1, with slightly higher values for Arm. Finally the transition metals, with highest *D* values, show variable preference for either Ilm–Gk or Arm.

D values for trace elements in both minerals show no significant change with increasing *P* in the small pressure range covered by our experiments. There is an increase in incompatibility from the HREE to the LREE for both Ilm–Gk and Arm. The incompatibility of the HFSE varies, with Th and U, and W to a lesser extent, being strongly incompatible, whilst Hf, Zr, Nb and Ta are only mildly incompatible. Both minerals preferentially incorporate U over Th. Ilm–Gk and Arm can fractionate the HFSE as $D_{Ta} > D_{Nb}$ and $D_{Hf} > D_{Zr}$. D_{Ta}/D_{Nb} is 1.54–1.59 for Ilm–Gk and 1.29–1.46 for Arm, D_{Hf}/D_{Zr} gives 1.39–1.44 for Ilm–Gk and 1.28–1.43 for Arm. Both Ilm–Gk and Arm also significantly fractionate W from Hf and D_{Hf}/D_W is 6.7–7.5 for Ilm–Gk and 11.9–12.9 for Arm. Finally for D_{Lu}/D_{Hf} we find 0.24–0.25 for the produced Ilm–Gk and 0.05–0.06 for Arm.

For the transition metals V, Cr and Cu we find $D > 1$ for both Ilm–Gk and Arm. Cr ($D_{Cr} = 7.5 \pm 1.2$) is the most compatible element in Ilm–Gk and V ($D_V = 8.1 \pm 1.3$) in Arm under these experimental conditions. An additional minor difference between Ilm–Gk and Arm is that $D_{Mn} > 1$ in Ilm–Gk, while Mn is incompatible in Arm.

Table 5
Ilm–Gk/melt and Arm/melt partition coefficients for experiments 1 and 3.

Exp.	1		3	
Phase	Ilm–Gk	Arm	Ilm–Gk	Arm
Sc	0.94(11)	1.65(2)	0.73(3)	1.5(1)
V	4.2(8)	9.2(19)	4.2(5)	6.9(7)
Cr	7.1(10)	6.4(10)	7.8(14)	6.7(12)
Mn	1.2(2)	0.34(5)	1.1(3)	0.34(11)
Co	2.5(5)	1.2(2)	2.3(9)	1.0(25)
Cu	2.9(7)	3.9(8)	2.3(7)	2.2(7)
Y	0.024(7)	0.019(10)	0.012(2)	0.0086(22)
Zr	0.23(3)	0.58(8)	0.17(3)	0.54(9)
Nb	0.52(9)	0.68(8)	0.40(5)	0.67(13)
Mo	0.93(24)	0.89(16)	0.60(10)	0.69(16)
Ba	0.035	0.010(3)	0.0014	0.0032(4)
La	0.0030(12)	0.0071(43)	0.0010(4)	0.0025(5)
Ce	0.0020(14)	0.010(4)	0.00062(42)	0.0029(6)
Nd	<0.0024	0.0085(24)	0.00077(39)	0.0032(12)
Sm	0.0089	<0.0071	0.0026(9)	<0.0034
Eu	0.0045(21)	0.013(4)	0.0015(7)	0.0028(9)
Er	0.030(14)	0.015(3)	0.019(4)	0.012(3)
Tm	0.044(14)	0.018(5)	0.028(3)	0.016(2)
Yb	0.059(17)	0.029(8)	0.0045(7)	0.023(3)
Lu	0.079(21)	0.049(19)	0.058(10)	0.032(3)
Hf	0.33(5)	0.83(13)	0.23(5)	0.69(9)
Ta	0.83(10)	0.99(9)	0.62(9)	0.86(10)
W	0.044(10)	0.065(14)	0.034(5)	0.058(12)
Th	0.0021(14)	0.0070(36)	0.00043(23)	0.0026(7)
U	0.0050(24)	0.011(3)	0.0019(5)	0.0046(10)

Numbers in parentheses indicate one standard deviation (1σ) of replicate analyses in terms of last significant numbers: 0.94(11) should be read as 0.94 ± 0.11. Note: Ba and LREE D values are likely affected by glass contamination and partition coefficients are therefore maximum values. We suggest using the lattice strain model parameters given in Table 6 to calculate D values for these elements for use in petrogenetic modelling.

In Fig. 5, Ilm–Gk/melt and Arm/melt partition coefficients for nominally di- tri- and tetravalent elements are shown as symbols in Onuma diagrams (Onuma et al., 1968) of log(D) values versus trace element radii (sixfold coordinated values from Shannon, 1976). Best-fit values for lattice strain parameters D_0, r_0 and E (Eq. (1)) are given in Table 6, and resulting crystal lattice strain model fits are shown as curves in Fig. 5.

4. DISCUSSION

4.1. Lattice strain models

Application of the lattice strain model (Table 6;Fig. 5) enables us to elucidate the substitution mechanism for some of the trace elements involved, and identify and correct for minor contamination issues affecting measured D values for highly incompatible elements. Fig. 5b shows that Ilm–Gk/melt and Arm/melt partitioning data for many nominally M^{3+} elements conform to the near-parabolic shape predicted from the lattice strain model. Partition coefficients for Cr and V are higher than expected for a purely M^{3+} element, consistent with both being multivalent (e.g. Papike et al. 2005). Deviations from the curves for the LREE D values are discussed below. Previous work has suggested that even the smallest M^{3+} cation considered here (Al) substitutes onto the Fe/Mg site in armalcolite (Smyth, 1974), not onto the smaller Ti site, and fits to the M^{3+} partitioning data are consistent with this suggestion for both Ilm–Gk and Arm.

The fits to our M^{3+} data reveal a minor contamination issue with our data. The LREE show higher partition coefficients than expected from the lattice strain model (Fig. 5b). As discussed by van Westrenen et al. (2001a) very small (<1 wt.%) amounts of glass contamination during trace element analysis of crystals can lead to significant overestimation of D values for highly incompatible elements. In Fig. 6 we show the effect of the addition of different percentages of glass to the Ilm–Gk mineral analysis for the 1.1 GPa experiment. The difference between observed and predicted D values for the LREE can be explained by as little as 0.1–0.3 wt.% glass contamination of our mineral analyses. Fig. 6 also shows that the effect of such minor addition on D values is minimal for the HREE. The LREE D values listed in Table 5 are therefore maximum values, and petrogenetic models involving LREE partitioning in the presence of Ilm–Gk and Arm should make use of D values calculated from the curves in Fig. 5b (using the parameters listed in Table 6).

The smaller group of partition coefficients for the divalent cations conforms partly to the lattice strain model (Fig. 5a). Comparing best-fit lattice strain model parameters shows that r_0 for divalent cations in Ilm–Gk is very close to the sixfold radius of Fe (0.78 Å, Shannon, 1976)

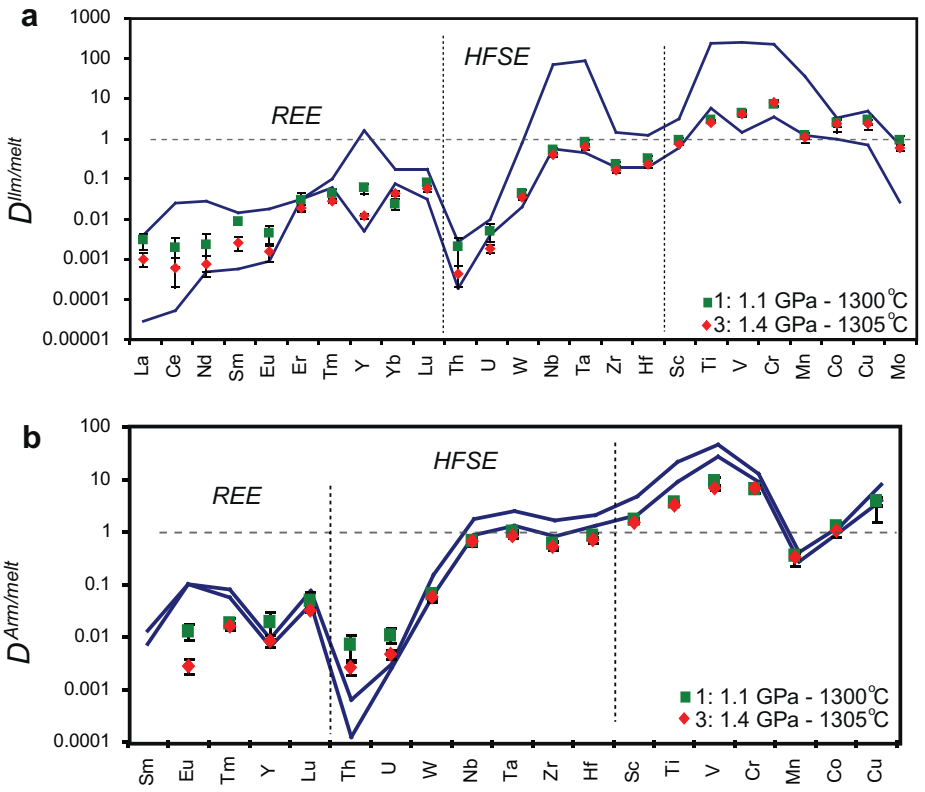

Fig. 3. Compilation of partition coefficients D_i for Ilm/Gk (a) and Arm (b) determined in this study and literature data (shown as lines representing upper and lower limits). For armalcolite not all experimentally determined D's from this study are included since no literature data was available for comparison for many elements. Literature generally uses Ilmenite while generally ilmenite–geikielite minerals were studied. For armalcolite trace element partitioning data presented in Klemme et al. (2006) for ferropseudobrookite was incorporated when a MgO was present. Data are from Green et al. (1971), McKay and Weill (1976), Palme and Wlotzka (1977), Irving et al. (1978), Fujimaki and Tatsumoto, 1984), McKay et al. (1986), Nakamura et al. (1986), Candela and Bouton (1990), LaTourrette et al., 1991), Stimac and Hickmott (1994), Zack and Brumm (1998), Klemme et al. (2006). For Er (Ilm–Gk) and Eu (Arm) only one study was available, therefore minimum and maximum values are equal.

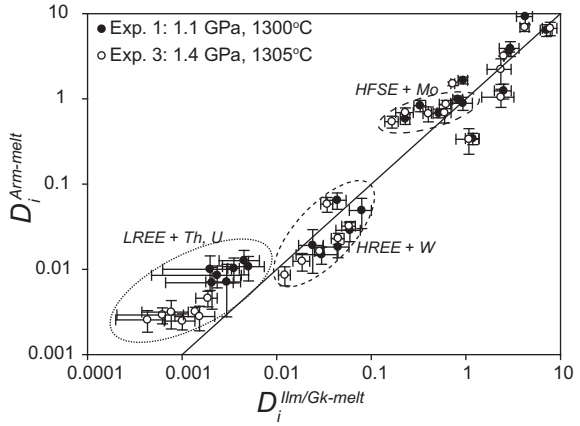

Fig. 4. Comparison between mineral–melt partition coefficients for Ilm–Gk and co-existing Arm. Unmarked elements are the transition metals.

whereas r_0 for Arm is closer to that of Mg (0.72 Å). This indicates substitution of M^{2+} into the Fe/Mg site. E values for divalent cations are identical within error for Ilm–Gk and Arm, suggesting the elastic properties of the sites in these two minerals are similar. E values are high compared to values for M^{2+} replacing divalent major cations in other minerals, which are generally in the range of 100–250 GPa (e.g. Blundy and Wood, 1994), suggesting the Fe/Mg sites in Ilm–Gk and Arm impose larger fractionations between divalent elements than these other minerals.

The minor contamination during laser ablation analysis identified from M^{3+} partitioning data also explains the discrepancy between the measured values of Ilm–Gk/melt and Arm/melt D_{Ba} and for Arm/melt D_{Ca} and values expected from lattice strain modelling. Glass contributions of 0.3–0.7 wt.% to the ilmenite–geikielite and armalcolite concentration measurements are sufficient to explain these unexpectedly high values. Copper and Co D values do not conform to the M^{2+} curve, as observed previously in both computer simulations and experiments on olivine–melt partitioning of M^{2+} cations (Purton et al., 2000). This is possibly due to Jahn–Teller effects in the case of Cu, and crystal field stability energy effects in crystals and melts in the case of Co, which affect overall partitioning energetics (Purton et al., 2000).

For both minerals r_0 for the tetravalent cations Si, Ti, Hf and Zr is close to that of Ti (0.605 Å), indicating that these elements preferentially substitute for Ti^{4+} (Fig. 5c). The

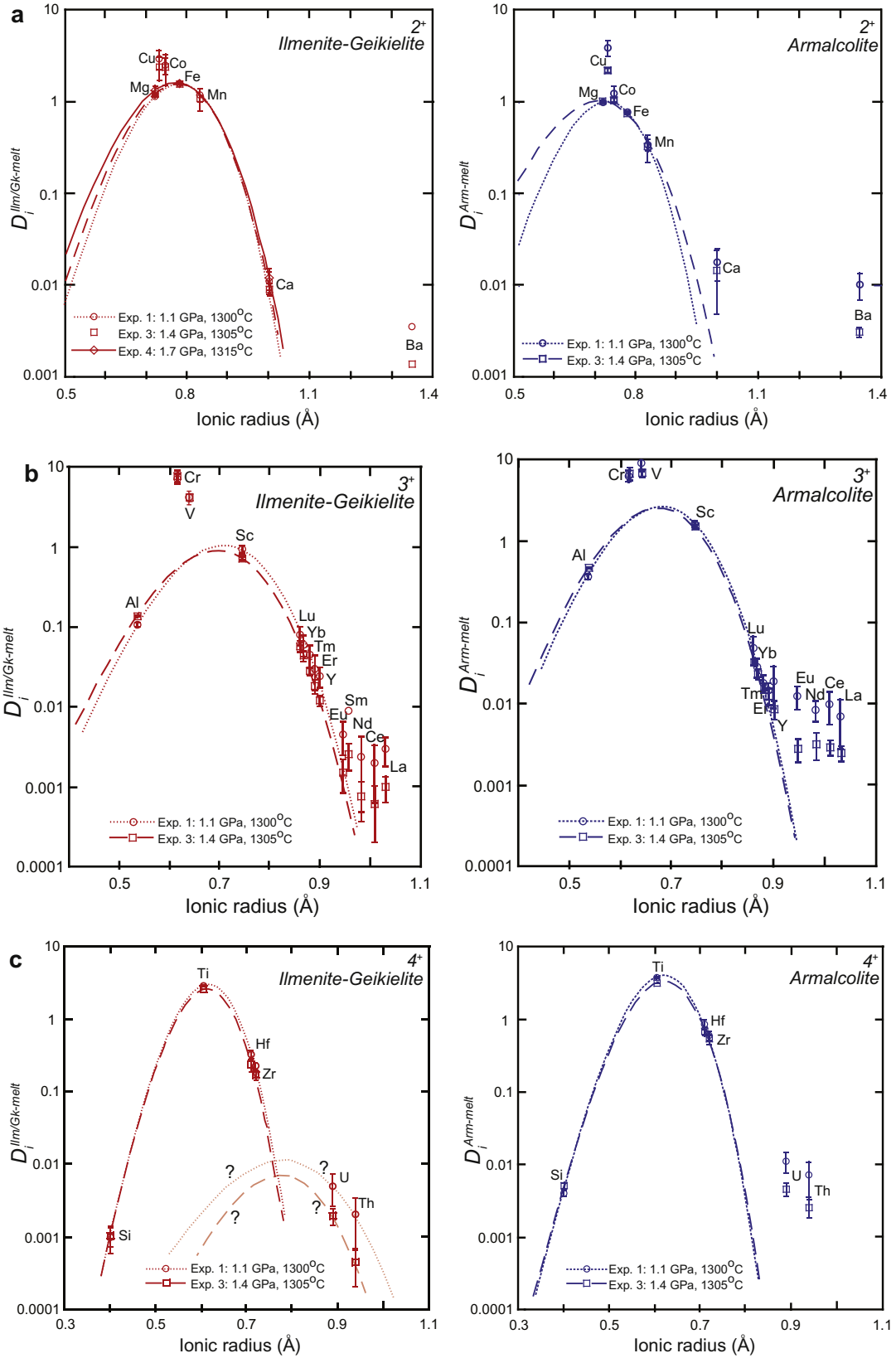

Fig. 5. Onuma diagrams showing mineral–melt partitioning data for the ilmenite–geikielite (left) and armalcolite (right) bearing experiments. (a) Nominally divalent elements; (b) nominally trivalent elements and (c) nominally tetravalent elements.

Table 6
Best fit values for lattice strain parameters D_0, E and r_0 for ilmenite–geikielite/melt and armalcolite/melt partition coefficients.

Exp.	1		3		4
P(GPa), T (°C)	1.1, 1300		1.4, 1305		1.7, 1315
Phase	Ilm–Gk	Arm	Ilm–Gk	Arm	Ilm–Gk
D_0					
2^+	1.58(3)	1.00(2)	1.55(2)	1.05(3)	1.58(5)
3^+	1.08(12)	2.65(24)	0.904(43)	2.59(13)	-
4^+	2.98(10)	3.87(13)	2.56(3)	3.32(4)	-
E					
2^+	410(70)	453(121)	382(11)	308(205)	347(38)
3^+	455(24)	536(21)	429(10)	528(11)	-
4^+	1243(46)	1014(21)	1260(38)	972(20)	-
r_0					
2^+	0.781(5)	0.730(7)	0.775(2)	0.711(27)	0.769(12)
3^+	0.707(2)	0.682(2)	0.696(1)	0.674(1)	-
4^+	0.617(2)	0.623(2)	0.614(2)	0.621(2)	-

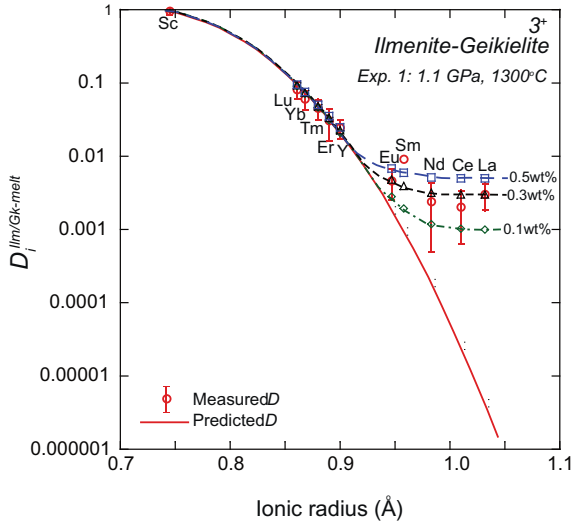

Fig. 6. Onuma diagram showing predicted lattice strain model-based partitioning curve for the trivalent elements (excluding Al and Cr) for the ilmenite–geikielite experiment at 1.1 GPa (solid line using values from Table 6) and the calculated effect of 0.1, 0.3 and 0.5 wt.% glass contamination of mineral analyses on this curve. Resulting effects on measured D values are large for the LREE, but minimal for the HREE. LREE D values are consistent with ~0.3 wt.% glass contamination during mineral analyses.

measured partition coefficients for U and Th are 3–4 orders of magnitude higher than expected from extrapolation of the lattice strain models for the other M^{4+} elements. The minor contamination issue discussed above cannot explain this large difference. This suggests that Th and U are incorporated into the larger Mg/Fe site in Ilm–Gk and Arm, rather than replacing Ti, similar to the situation in Ti-rich garnets (Van Westrenen et al., 2001b).

Most best-fit lattice strain parameters show little or no variation across the pressure range covered in these experiments. The only exceptions are the observed slight decreases in r_0 for divalent cations with increasing pressure for both Ilm–Gk and Arm, accompanied by small decreases in apparent site Young's moduli E. Decreases in r_0 with increasing P have been observed in partitioning data for other minerals (most notably garnet, e.g. Draper and van Westrenen, 2007; van Westrenen and Draper, 2007) and are consistent with the measured decreases in the Mg/Fe site volumes with increasing compression (e.g. Tronche et al., 2010). Although decreases in r_0 are often accompanied by *in*creases in E, interpreting E values is notoriously difficult (e.g. Hill et al., 2000; van Westrenen et al., 2000) and our data set is too small to draw definitive conclusions about the relation between r_0 and E for divalent cations in Arm and Ilm–Gk.

4.2. Implications for Lu–Hf–Ti concentrations of lunar high-Ti mare basalts

Because of the bulk composition and conditions used, the partition coefficients presented in this study are directly relevant to the Moon. A variety of models have been proposed to explain the high Ti contents of these basalts, including assimilation of late-stage ilmenite-bearing cumulates by low-Ti ultramafic liquids at shallow levels (e.g. Anderson, 1971; Hubbard and Minear, 1975; Wagner and Grove, 1997), sinking of late stage ilmenite cumulates to form a deep hybrid mantle source (e.g. Ringwood and Kesson, 1976; Hess and Parmentier, 1995) and shallow-level reaction and mixing of cumulates, followed by sinking of hybrid high-Ti material (Van Orman and Grove, 2000). In addition, Nakamura et al. (1986) and Beard et al. (1998) showed that the Lu/Hf ratios of high-Ti mare basalts (Lu/Hf = 0.12–0.17) are significantly lower than chondritic (Lu/Hf = 0.21, Lodders, 2003), requiring the addition of a mineral that preferentially incorporates Hf over Lu. Ilm–Gk (D_{Lu}/D_{Hf} = 0.24–0.25) and Arm (D_{Lu}/D_{Hf} = 0.05–0.06) are such minerals, they are the only minerals involved in lunar magma ocean (LMO) crystallisation that preferentially incorporate Hf over Lu. Partitioning studies of other minerals that played a role during lunar magmatic processes all show $D_{Lu}/D_{Hf} > 1$. For example, olivine shows

Table 7
Input parameters for trace element evolution modelling during LMO crystallisation assuming the crystallisation model of Snyder et al. (1992).

Concentrations					Partition coefficients					
	LMO_i[a]	High Ti[b1]	High Ti[b2]	High Ti[b3]	D_{OL}[c]	D_{OPX}[d]	D_{CPX}[c]	D_{Plag}[e]	D_{Ilm-gk}[f]	D_{Arm}[f]
Lu (ppm)	0.119	1.0–1.1	2.4–2.6	0.5–1.5	0.041	0.052	0.74	0.0018	0.079	0.049
Hf (ppm)	0.575	6.4–7.0	14.7–15.9	5.1–10	0.013	0.0086	0.37	0.001	0.33	0.83
TiO_2 (wt.%)		12.5–13.7	9.1–9.7	10.1–14.2	0.010	0.071	0.34	0.0446	2.9	3.7
Lu/Hf	**0.21**	**0.16**	**0.16–0.17**	**0.13–0.17**	**3.2**	**6.1**	**2.0**	**1.8**	**0.24**	**0.06**

[a] Initial values for the Lu and Hf concentrations in the LMO (LMO_i = 5*CI chondrites) are derived using CI values of Lodders (2003).
[b] Lu–Hf and TiO_2 concentrations from Beard et al. (1998) for Apollo 17 basalts (b1) and Apollo 11 basalts (b2), and from Warner et al. (1979) for Apollo 17 basalts (b3).
[c] Partition coefficients for OL and CPX from McDade et al. (2003).
[d] Partition coefficients for OPX from van Kan Parker et al. (2011).
[e] Partition coefficients for Plag from Tepley et al. (2010), with D_{Lu} fitted using the lattice strain model.
[f] Partition coefficients for Ilm-Gk and Arm are from Experiment 1 (this study).

$D_{Lu}/D_{Hf} = 3.2$ (McDade et al., 2003), clinopyroxene $D_{Lu}/D_{Hf} = 2.0$ (e.g. McDade et al., 2003), plagioclase $D_{Lu}/D_{Hf} = 1.8$ (e.g. Tepley et al., 2010) and orthopyroxene $D_{Lu}/D_{Hf} = 6.1 \pm 2.5$ (van Kan Parker et al., 2011).

We calculated the Lu–Hf–Ti evolution of a crystallising LMO and corresponding cumulates, assuming the LMO crystallisation model of Snyder et al. (1992). This model is based on calculations using the olivine–plagioclase–silica ternary phase diagram at 0.6 GPa derived from experiments performed by Longhi (1981). It assumes that, due to vigorous convection in the magma ocean, the first three quarters of LMO crystallisation were characterised by equilibrium crystallisation during which olivine and later orthopyroxene crystallised. During the last quarter of crystallisation, when convection efficiency is lower due to the presence of crystals, it is assumed that fractional crystallisation was dominant with crystallisation of clinopyroxene, pigeonite, plagioclase, olivine and finally ilmenite. In this model ilmenite is assumed to have started crystallising from $\geqslant$95%. The partition coefficients we used for all minerals involved in LMO crystallisation, including our new data, are summarised in Table 7. Following Snyder et al. (1992) and Münker (2010) we assume 5 × C1 chondrite values for initial LMO Lu and Hf concentrations.

During initial magma ocean crystallisation Lu/Hf decreases in the residual liquids due to the high D_{Lu}/D_{Hf} ratios of the crystallising minerals, and the corresponding cumulates containing Ol ± Opx ± Cpx ± Plag show superchondritic Lu/Hf ratios, between 0.36 and 1.2. Ilmenite and/or armalcolite start crystallising when the LMO has solidified for >95% (Snyder et al., 1992). We test models in which the Ti-rich minerals continue crystallising up to a total of 98% or 99% total LMO crystallisation. Consistent with Snyder et al. (1992) the late stage Ti-rich minerals crystallise together with clinopyroxene and plagioclase, producing a so-called ilmenite bearing cumulate layer (IBCL) or an equivalent armalcolite-bearing cumulate layer (ABCL). Using our partition coefficients the Lu/Hf ratios of ilmenite are predicted to be subchondritic in the range of 0.025–0.034, while armalcolite shows Lu/Hf ratios of 0.0068–0.0084. Lutetium/Hf ratios of bulk IBCL and ABCL vary between super- and subchondritic, respectively (Fig. 7), dependant on the total amount of crystallisation of the LMO. At $\geqslant$99% crystallisation, bulk Lu/Hf of IBCL and ABCL are not as subchondritic as the observed ratios in the high-Ti mare basalts.

Fig. 7 shows predicted Lu–Hf–Ti concentrations for models whereby high-Ti basalts are generated by partially melting (10% fractional melting) the Opx cumulate formed

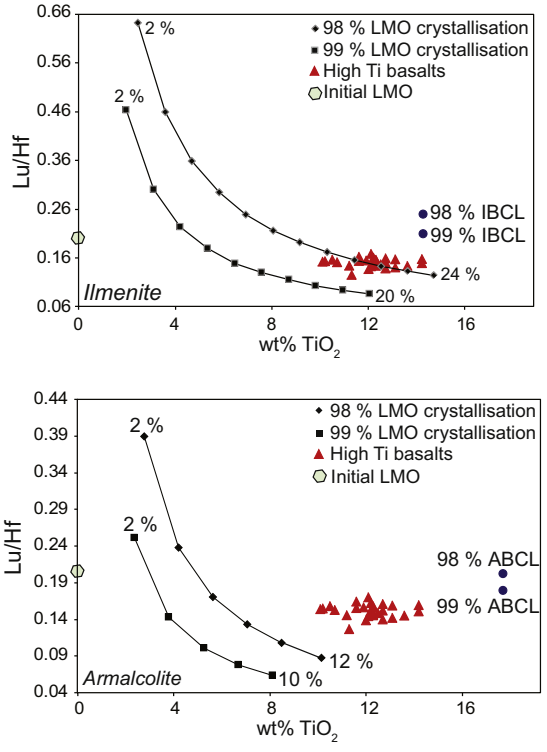

Fig. 7. Comparison between observed (triangles, compilation from Beard et al., 1998 and Warner et al., 1979) and modelled (this study) Lu/Hf ratios and TiO_2 contents of high-Ti mare basalts. Curves show progressive dissolution of (a) ilmenite–geikielite or (b) armalcolite into 10% partial melts of early orthopyroxene cumulates. The Lu/Hf ratio of these initial melts decreases steeply with increasing Ilm (a) or Arm (b) addition. The Lu/Hf ratios of bulk ilmenite bearing cumulate (IBCL) and bulk armalcolite bearing cumulate (ABCL) are shown assuming Ti-rich mineral crystallisation up to either 98% or 99% total solidification of the LMO.

during early LMO crystallisation, followed by shallower-level dissolution of Ilm–Gk or Arm from late-stage cumulate remnants. When we assume Ilm–Gk crystallisation up to 98% LMO solidification, a mixture of 17% of dissolved ilmenite with 83% of cumulate partial melt is required to reproduce the observed Lu/Hf ratio of 0.16 in the high-Ti mare basalts (Fig. 7a). If armalcolite would crystallise instead of ilmenite a mixture of ~6.5% of armalcolite and ~93.5% of cumulate partial melt is sufficient (Fig. 7b). If Ti-rich mineral crystallisation from the LMO would continue up to 99% of solidification the required proportions reduce to ~9% for ilmenite and to ~3.5% if armalcolite dissolution is involved. A robust result from our modelling is that bulk dissolution of the IBCL or the equivalent ABCL including clinopyroxene and/or plagioclase cannot reproduce the observed subchondritic Lu/Hf ratios since their Lu/Hf ratios are higher than observed in the basalts. Selective dissolution of the Ti-rich phase is therefore required, consistent with the dissolution modelling of Wagner and Grove (1997).

These scenarios reproduce the observed Lu/Hf ratio and the absolute TiO_2 concentrations in the high-Ti mare basalts. Absolute concentrations for Lu and Hf in these models are lower than the measured values. Simple late-stage olivine ± orthopyroxene fractionation at shallow levels, using the partition coefficients listed in Table 7, would result in higher absolute values of both Lu and Hf at virtually unchanged Lu/Hf ratios. However, TiO_2 concentrations would simultaneously increase to levels far exceeding those observed. Alternatively, shallow-level fractionation of olivine ± ilmenite, or olivine ± armalcolite (as suggested by, e.g. Longhi, 1992) would lower TiO_2 concentrations to levels below those observed.

Fractionation of olivine ± orthopyroxene ± ilmenite would only change TiO_2 concentrations to a very minor extent while increasing the absolute Lu and Hf concentrations. This latter scenario would also increase the Lu/Hf ratio slightly and therefore slightly more initial ilmenite dissolution would be required (18% at 98% crystallisation of the LMO, or 10% at 99% crystallisation of the LMO). We stress however that this analysis assumes that the partition coefficients listed in Table 7, chosen for their applicability during high-pressure processes, are equally valid at low pressure – an assumption that remains to be tested experimentally.

5. CONCLUSIONS

We have experimentally determined the partitioning behaviour of a wide range of trace elements between ilmenite, armalcolite and anhydrous lunar silicate melt at high pressure and temperature in a Ti-rich system, to constrain geochemical models of the evolution of the interior of the Moon. Our data enable us to quantitatively model the Lu–Hf–Ti concentrations of lunar high-Ti basalt. We show that the combination of subchondritic Lu/Hf ratios and high TiO_2 contents requires preferential dissolution of ilmenite or armalcolite from late-stage lunar magma ocean cumulates into low-Ti partial melts of deeper pyroxene-rich cumulates, followed by shallow fractionation of olivine ± orthopyroxene ± ilmenite.

ACKNOWLEDGEMENTS

We would like to thank two anonymous reviewers, Jane Chadwick, Tim Grove, Mike Krawczynski and Bjorn Mysen for their insightful reviewer comments. We like to thank Helen de Waard for assistance with the LA-ICP-MS measurements, and the VU University Amsterdam mechanical and electronic workshops for supporting the high pressure laboratory. Laser ablation ICP-MS instrumentation at Utrecht University was supported by an investment grant from the Netherlands Organization for Scientific Research (NWO). This research was funded through a European Science Foundation EURYI award to W. van W.

REFERENCES

Anderson A. T. (1971) Exotic armalcolite and the origin of Apollo 11 ilmenite basalts. *Geochimica et Cosmochimica Acta* **35**, 969–970.

Beard B. L., Taylor L. A., Scherer E. E., Johnson C. M. and Snyder G. A. (1998) The source region and melting mineralogy of high-titanium and low-titanium lunar basalts deduced from Lu–Hf isotope data. *Geochimica et Cosmochimica Acta* **62**, 525–544.

Beck A. R. and Hess P. C. (2004) Ilmenite solubility in Lunar basalts as a function of temperature and pressure: Implications for petrogenesis. *Lunar and Planetary Science Conference* **35**, 1807.

Blundy J. and Wood B. (1994) Prediction of crystal-melt partition-coefficients from elastic-moduli. *Nature* **372**, 452–454.

Candela P. A. and Bouton S. L. (1990) The influence of oxygen fugacity on tungsten and molybdenum partitioning between silicate melts and ilmenite. *Economic Geology and the Bulletin of the Society of Economic Geologists* **85**, 633–640.

de Vries J., van den Berg A. and van Westrenen W. (2010) Formation and evolution of a lunar core from ilmenite-rich magma ocean cumulates. *Earth and Planetary Science Letters* **292**, 139–147.

Delano J. W. (1986) Pristine lunar glasses – criteria, data, and implications. *Journal of Geophysical Research-Solid Earth and Planets* **91**, D201–D213.

Dorrit E. J. (2006) High sensitivity analysis of trace element-poor geological reference glasses by laser ablation-inductively coupled plasma-mass spectrometry (LA-ICP-MS). *Geostandards and Geoanalytical Research* **30**, 221–235.

Draper D. S. and van Westrenen W. (2007) Quantifying garnet-melt trace element partitioning using lattice-strain theory: assessment of statistically significant controls and a new predictive model. *Contributions to Mineralogy and Petrology* **154**, 731–746.

Dygert N., Liang Y. and Hess P. C. (2011) Experimental evidence for high field strength element incorporation in titaniferous phases in equilibrium with high titanium mare basalts. *Lunar and Planetary Science Conference* **42**, 1956.

Elardo S. M., Draper D. S. and Shearer C. K. (2011) Lunar magma ocean crystallization revisited: bulk composition, early cumulate mineralogy, and the source regions of the highlands Mg-suite. *Geochimica et Cosmochimica Acta* **75**, 3024–3045. doi:10.1016/j.gca.2011.02.033.

Elkins-Tanton L. T., Van Orman J. A., Hager B. H. and Grove T. L. (2002) Re-examination of the lunar magma ocean cumulate

overturn hypothesis: melting or mixing is required. *Earth and Planetary Science Letters* **196**, 239–249.

Friel J. J., Harker R. I. and Ulmer G. C. (1977) Armalcolite stability as a function of pressure and oxygen fugacity. *Geochimica et Cosmochimica Acta* **41**, 403–410.

Fujimaki H. and Tatsumoto M. (1984) Lu–Hf constraints on the evolution of lunar basalts. *Journal of Geophysical Research* **89**, B445–B458.

Green D. H., Ringwood A. E., Ware N. G., Hibberson W. O., Major A. and Kiss E. (1971) Experimental petrology and petrogenesis of Apollo 12 basalts. *Proceedings Lunar Planetary Science Conference* **2**(1), 601–615.

Günther D., Frischknecht R., Heinrich C. A. and Kahlert H.-J. (1997) Capabilities of an argon fluoride 193 nm excimer laser for laser ablation inductively coupled plasma mass spectrometry microanalysis of geological materials. *Journal of Analytical Atomic Spectrometry* **12**, 939–944.

Hess P. C. and Parmentier E. M. (1995) A model for the thermal and chemical evolution of the Moons interior – implications for the onset of mare volcanism. *Earth and Planetary Science Letters* **134**, 501–514.

Hill E., Wood B. J. and Blundy J. D. (2000) The effect of Ca-Tschermaks component on trace element partitioning between clinopyroxene and silicate melt. *Lithos* **53**, 203–215.

Horng W. S. and Hess P. C. (2000) Partition coefficients of Nb and Ta between rutile and anhydrous haplogranite melts. *Contributions to Mineralogy and Petrology* **138**, 176–185.

Hubbard N. J. and Minear J. W. (1975) A chemical and physical model for the genesis of lunar rocks: part II Mare basalts. *Proceedings of the Lunar Science Conference* **6**, 405–407.

Irving A. J., Merrill R. B. and Singleton D. E. (1978) Experimental partitioning of rare earth elements and scandium among armalcolite, ilmenite, olivine, and mare basalt liquid. *Proceedings Lunar Planetary Science Conference* **9**, 601–612.

Jochum K. P. and Brueckner S. M. (2008) Reference materials in geoanalytical and environmental research – review for 2006 and 2007. *Geostandards and Geoanalytical Research* **32**, 405–452.

Klemme S., Günther D., Hametner K., Prowatke S. and Zack T. (2006) The partitioning of trace elements between ilmenite, ulvospinel, annalcolite and silicate melts with implications for the early differentiation of the moon. *Chemical Geology* **234**, 251–263.

Krawczynski M. J. and Grove T. L. (2008) Experimental investigations of fO_2 effects on Apollo 17 orange glass phase equilibria. *Lunar Planetary Science Conference* **39**, 1231.

LaTourrette T. Z., Burnett D. S. and Bacon C. R. (1991) Uranium and minor-element partitioning in Fe–Ti oxides and zircon from partially melted granodiorite, Crater Lake Oregon. *Geochimica et Cosmochimica Acta* **55**, 457–469.

Lee D.-C., Halliday A. N., Leya I., Wieler R. and Wiechert U. (2002) Cosmogenic tungsten and the origin and earliest differentiation of the Moon. *Earth and Planetary Science Letters* **198**, 267–274.

Liang Y. and Hess P. C. (2008) Preferential assimilation of armalcolite, ilmenite, and pyroxene during melt migration in the lunar mantle can produce the two linear arrays observed in pristine lunar glass melts. *Lunar and Planetary Science Conference* **39**, 2083.

Liang Y., Lo Cascio M. and Hess P. C. (2007) Preferential assimilation of armalcolite and ilmenite during melt migration and melt-rock reaction in the lunar mantle: an experimental study. *Lunar and Planetary Science Conference* **38**, 1075.

Lodders K. (2003) Solar system abundances and condensation temperatures of the elements. *Astrophysical Journal* **591**, 1220–1247.

Longhi J. (1981) Preliminary modeling of high pressure partial melting: implications for early lunar differentiation. *Proceedings of Lunar Planetary Science Conference*, 1001–1018.

Longhi J. (1992) Experimental petrology and petrogenesis of mare volcanics. *Geochimica et Cosmochimica Acta* **56**, 2235–2251.

Lucey P., Korotev R. L., Gillis J. J., Taylor L. A., Lawrence D., Campbell B. A., Elphic R., Feldman B., Hood L. L., Hunten D., Mendillo M., Noble S., Papike J. J., Reedy R. C., Lawson S., Prettyman T., Gasnault O. and Maurice S. (2006) Understanding the lunar surface and space-moon interactions. *Reviews in Mineralogy and Geochemistry* **60**, 83–219.

McDade P., Blundy J. D. and Wood B. J. (2003) Trace element partitioning on the Tinaquillo Lherzolite solidus at 1.5 GPa. *Physics of the Earth and Planetary Interiors* **139**, 129–147.

McKay G. A. and Weill D. F. (1976) Application of major and trace element crystal/liquid partitioning to the origin of KREEP. *Lunar and Planetary Science Conference* **7**, 527–529.

McKay G., Wagstaff J. and Yang S. R. (1986) Zirconium, hafnium, and rare-earth element partition-coefficients for ilmenite and other minerals in high-Ti lunar mare basalts – an experimental-study. *Journal of Geophysical Research-Solid Earth and Planets* **91**, D229–D237.

Médard E., McCammon C. A., Barr J. A. and Grove T. L. (2008) Oxygen fugacity, temperature reproducibility, and H_2O contents of nominally anhydrous piston-cylinder experiments using graphite capsules. *American Mineralogist* **93**, 1838–1844.

Münker C. (2010) A high field strength element perspective on early lunar differentiation. *Geochimica et Cosmochimica Acta* **74**, 7340–7361.

Mysen B. O. and Shang J. (2005) Evidence from olivine/melt element partitioning that non-bridging oxygen in silicate melts are not equivalent. *Geochimica et Cosmochimica Acta* **69**, 2861–2875.

Mysen B. O. and Dubinsky E. V. (2004) Melt structural control on olivine/melt element partitioning of Ca and Mn. *Geochimica et Cosmochimica Acta* **68**, 1617–1633.

Nakamura Y., Fujimaki H., Nakamura N., Tatsumoto M., McKay G. A. and Wagstaff J. (1986) Hf, Zr, and REE partition-coefficients between ilmenite and liquid – implications for lunar petrogenesis. *Journal of Geophysical Research-Solid Earth and Planets* **91**, D239–D250.

Neal C. R. and Taylor L. A. (1992) Petrogenesis of mare basalts: a record of lunar volcanism. *Geochimica et Cosmochimica Acta* **56**, 2177–2211.

Nicholis M. G. and Rutherford M. J. (2009) Graphite oxidation in the Apollo 17 orange glass magma: implications for the generation of a luinar volcanic gas phase. *Geochimica et Cosmochimica Acta* **73**, 5905–5917.

Onuma N., Higuchi H., Wakita H. and Nagasawa H. (1968) Trace element partition between 2 pyroxenes and host lava. *Earth and Planetary Science Letters* **5**, 47–51.

Palme H. and Wlotzka F. (1977) Trace element fractionation during crystallization of lunar rock 75035. *Lunar and Planetary Science Conference* **8**, 747–749.

Papike J. J., Karner J. M. and Shearer C. K. (2005) Comparative planetary mineralogy: valence state partitioning of Cr, Fe, Ti, and V among crystallographic sites in olivine, pyroxene, and spinel from planetary basalts. *American Mineralogist* **90**, 277–290.

Pearce N. J. G., Perkins W. T., Westgate J. A., Gorton M. P., Jackson S. E., Neal C. R. and Chenery S. P. (1997) A compilation of new and published major and trace element data for NIST SRM 610 and NIST SRM 612 glass reference materials. *Geostandards Newsletter – the Journal of Geostandards and Geoanalysis* **21**, 115–144.

Pertermann M., Hirschmann M. M., Hametner K., Günther D. and Schmidt M. W. (2004) Experimental determination of trace element partitioning between garnet and silica-rich liquid during anhydrous partial melting of MORB-like eclogite. *Geochemistry Geophysics Geosystems* **5**. doi:10.1029/2003GC000638.

Press, W. H., Teukolsky, S. A., Vetterling, W. T. and Flannery, B. P. (1992) *Numerical Recipes in C*. 2nd ed. Cambridge University Press, Cambridge, 965p.

Purton J. A., Blundy J. D. and Allan N. L. (2000) Computer simulation of high-temperature, forsterite-melt partitioning. *American Mineralogist* **85**, 1087–1091.

Raymond K. N. and Wenk H. R. (1971) Lunar ilmenite (refinement of crystal structure). *Contributions to Mineralogy and Petrology* **30**, 135–140.

Reed S. J. B. (2005) *Electron microprobe analysis and scanning electron microscopy in geology*. Cambridge University Press, Cambridge, UK.

Righter K. and Shearer C. K. (2003) Magmatic fractionation of Hf and W: constraints on the timing of core formation and differentiation in the Moon and Mars. *Geochimica et Cosmochimica Acta* **67**, 2497–2507.

Ringwood A. E. and Kesson S. E. (1976) A dynamic model for mare basalt petrogenesis. *Proceedings Lunar Planetary Science Conference* **7**, 1697–1722.

Shannon R. D. (1976) Revised effective ionic-radii and systematic studies of interatomic distances in halides and chalcogenides. *Acta Crystallographica Section A* **32**, 751–767.

Shearer C. K. and Papike J. J. (1999) Magmatic evolution of the Moon. *American Mineralogist* **84**, 1469–1494.

Shearer C. K., Papike J. J. and Layne G. D. (1996) The role of ilmenite in the source regions for mare basalts: evidence from niobium, zirconium, and cerium in picritic glasses. *Geochimica et Cosmochimica Acta* **60**, 3521–3530.

Shearer C. K., Hess P. C., Wieczorek M. A., Pritchard M. E., Parmentier E. M., Borg L. E., Longhi J., Elkins-Tanton L. T., Neal C. R., Antonenko I., Canup R. M., Halliday A. N., Grove T. L., Hager B. H., Lee D.-C. and Wiechert U. (2006) Thermal and magmatic evolution of the Moon. *Reviews in Mineralogy and Geochemistry* **60**, 365–518.

Smith J., Anderson A., Newton R., Olsen E., Wyllie P., Crewe A., Isaacson M. and Johnson D. (1970) Petrologic history of the moon inferred from petrography, mineralogy, and petrogenesis of Apollo 11 rocks. *Geochimica et Cosmochimica Acta Suppl.* **1**, 897–925.

Smyth J. R. (1974) The crystal chemistry of armalcolites from Apollo 17. *Earth and Planetary Science Letters* **24**, 262–270.

Snyder G. A., Taylor L. A. and Neal C. R. (1992) A chemical-model for generating the sources of mare basalts – combined equilibrium and fractional crystallization of the lunar magmasphere. *Geochimica et Cosmochimica Acta* **56**, 3809–3823.

Stimac J. and Hickmott D. (1994) Trace-element partition-coefficients for ilmenite, ortho-pyroxene and pyrrhotite in rhyolite determined by micro-pixe analysis. *Chemical Geology* **117**, 313–330.

Tepley, III, F. J., Lundstrom C. C., McDonough W. F. and Thompson A. (2010) Trace element partitioning between high – an plagciolase and basaltic to basaltic andesite melt at 1 atmosphere pressure. *Lithos* **118**, 82–94.

Thacker C., Liang Y., Peng Q. and Hess P. (2009) The stability and major element partitioning of ilmenite and armalcolite during lunar cumulate mantle overturn. *Geochimica et Cosmochimica Acta* **73**, 820–836.

Tronche E. J., van Kan Parker M., de Vries J., Wang Y., Sanehira T., Li J., Chen B., Gao L., Klemme S., McCammon C. A. and van Westrenen W. (2010) The thermal equation of state of $FeTiO_3$ ilmenite based on *in situ* X-ray diffraction at high pressures and temperatures. *American Mineralogist* **95**, 1708–1716.

van Kan Parker, Mason, P., and van Westrenen (2011). Experimental study of trace element partitioning between lunar orthopyroxene and anhydrous silicate melt: effects of lithium and iron. *Chemical Geology*, doi:10.1016/j.chemgeo.2011.02.007.

Van Orman J. A. and Grove T. L. (2000) Origin of lunar high-titanium ultramafic glasses: Constraints from phase relations and dissolution kinetics of clinopyroxene–ilmenite cumulates. *Meteoritics & Planetary Science* **35**, 783–794.

van Westrenen W. and Draper D. S. (2007) Quantifying garnet-melt trace element partitioning using lattice-strain theory: new crystal-chemical and thermodynamic constraints. *Contributions to Mineralogy and Petrology* **154**, 717–730.

van Westrenen W., Allan N. L., Blundy J. D., Purton J. A. and Wood B. J. (2000) Atomistic simulation of trace element incorporation into garnets – comparison with experimental garnet-melt partitioning data. *Geochimica et Cosmochimica Acta* **64**, 1629–1639.

van Westrenen W., Wood B. J. and Blundy J. D. (2001a) A predictive thermodynamic model of garnet-melt trace element partitioning. *Contributions to Mineralogy and Petrology* **142**, 219–234.

van Westrenen, W., Blundy, J. D., and Wood, B.J. (2001b) HFSE/REE fractionation during partial melting in the presence of garnet: Implications for identification of mantle heterogeneities. *Geochemistry, Geophysics, Geosystems* **2**, 2000GC000133.

Wagner T. P. and Grove T. L. (1997) Experimental constraints on the origin of lunar high-Ti ultramafic glasses. *Geochimica et Cosmochimica Acta* **61**, 1315–1327.

Warner R. D., Taylor G. J., Conrad G. H., Northrop H. R., Barker S., Keil K., Ma M.-S. and Schmitt R. (1979) Apollo 17 high-Ti mare basalts: new bulk compositional data, magma types, and petrogenesis. *Proceedings of the Lunar and Planetary Science Conference* **10**, 225–247.

Watson E. B., Wark D. A., Price J. D. and Van Orman J. A. (2002) Mapping the thermal structure of solid-media pressure assemblies. *Contributions to Mineralogy and Petrology* **142**, 640–652.

Wood J., Dickey J., Marvin U. and Powell B. (1970) Lunar anorthosites and a geophysical model of the moon. *Geochimica et Cosmochimica Acta Suppl.* **1**, 965–988.

Zack T. and Brumm R. (1998) Ilmenite/liquid partition coefficients of 26 trace elements determined through ilmenite/clinopyroxene partitioning in garnet pyroxenites. *International Kimberlite Conference* **986**, 988.

Associate editor: Bjorn Mysen